Research article

Optical and water repellant properties of Ag/SnO$_2$ bilayer thin films

**Ravipati Praveena [1], Gottapu. Varaprasada Rao [1], Karna Balasubrahmanyam [1],
M. Ghanashyam Krishna [2],*, and Vinjanampati Madhurima [3]**

[1] Department of Physics, GVP College of Engineering (A), Visakhapatnam - 530 048, India

[2] Centre for Advanced Studies in Electronics Science and Technology, School of Physics, University of Hyderabad, Hyderabad-500 046, India

[3] Department of Physics, School of Basic and Applied Sciences, Central University of Tamil Nadu, Thiruvarur, Tamil Nadu - 610101, India

* Correspondence: Email: mgksp@uohyd.ac.in.

Abstract: The optical and water repellant properties of single layer and bilayer films of Ag and SnO$_2$ deposited on glass substrates by thermal evaporation have been reported. Ag/SnO$_2$ bilayers were deposited in two sequences wherein the deposition of SnO$_2$ layer was followed by Ag deposition and vice versa. X-ray diffraction studies show that the Ag films crystallize in the FCC structure and SnO$_2$ is amorphous, while atomic force microscopy images indicate the formation of large clusters of the order of 12 nm. The single layer Ag films exhibit localized surface plasmon resonance (LSPR) that shifts from visible region to the infrared with increase in thickness from 5 to 12 nm. It is observed that, only the Ag films of thickness ≤ 8 nm exhibits LSPR peak whereas the critical thickness is 5 nm for Ag/SnO$_2$ films. A blue shift is observed in the LSPR peak position when the SnO$_2$ layer caps the Ag film. Whereas, the LSPR of Ag is suppressed significantly when the SnO$_2$ layer is introduced between the glass and the Ag film and also when Ag and SnO$_2$ were co-evaporated. Water repellant properties indicate that the pure Ag film has an average contact angle of 104° which decreases to 100° when SnO$_2$ caps the Ag layer and 97° when Ag is deposited on top of the SnO$_2$ buffer layer. Co-evaporated Ag-SnO$_2$ films show a contact angle of 93°.

Keywords: Ag; SnO$_2$; metal-dielectric thin films; surface plasmon resonance; wettability

1. Introduction

Tin oxide (SnO$_2$) has attracted great attention in many applications such as solar cells, gas sensors, liquid crystal displays, optoelectronic devices, transparent conducting electrodes, liquid crystal displays, photocells, detectors, antireflection coatings, etc., because of its excellent electrical and optical properties, high optical transparency (350–900 nm), high chemical durability, low cost as a starting material, high exciton binding energy of 130 meV at room temperature and wide band gap (3.6 eV) [1–7]. Reports showed that Ag deposition on the SnO$_2$ surface can increase the sensor response in correlation with reducing gasses by more than 5–12 times [8]. Aguilar-Leyva et al. [7] prepared Ag/SnO$_2$ bilayer films for the detection of LPG gas and showed that the Ag/SnO$_2$ structure exhibit the highest sensitivity than SnO$_2$/Ag structures. Yu et al. [9,10] prepared high quality SnO$_2$/Ag/SnO$_2$ tri-layer films for transparent conducting applications.

It is well known that wetting properties of materials depend on their chemical nature, roughness and morphology. The role of the surface roughness has widely been studied and it has been found to have opposite effects: increasing the roughness of a chemically hydrophobic surface will enhance its hydrophobicity, while increasing the roughness of a hydrophilic surface will further enhance its hydrophilicity. It was shown that the metal layer and doping concentration influences the wettability properties significantly [11,12,13]. In addition, it was also reported that metal doped SnO$_2$ films had tunable optical and wettability properties. Transparent hydrophobic surfaces are quite important for a variety of applications [14–17], therefore in the present investigation the authors extended the study to the Ag/SnO$_2$ system and investigated the possibility of fabricating transparent water repellant Ag/SnO$_2$ thin films.

2. Materials and Method

Thin films of Ag and SnO$_2$ were deposited on glass substrates by resistive thermal evaporation carried out in vacuum better than 5×10^{-5} mbar and rate of deposition between 0.1–0.5 Å/s without intentionally heating the substrates. The glass substrates were first cleaned with acetone and ethanol and then rinsed with ethanol in an ultrasonic cleaner for 20 min prior to each deposition. Ag wire (99.9% Pure) and SnO$_2$ (99%) powder were placed in a tungsten spiral and molybdenum boats, respectively. The substrates were placed in the holder at a distance of 10 cm from the source. The substrates were retained in the same vacuum for 1 hour after completing the deposition process. Thickness of the films was measured using a quartz crystal thickness monitor.

For the single and bilayer films, transmission spectra were measured using a UV-VIS-NIR spectrophotometer (Elico model No. SL 159). Morphology of single and bilayer films was imaged using atomic force microscopy (AFM) operating in the non-contact DFM mode (SPA 400 of Seiko Instruments Inc., Japan). The crystal structure of the films was obtained from a powder X-ray diffractometer (Philips PW 1830 with Cu K$_\alpha$ radiation of wavelength 0.15406 nm). Contact angles and surface energy of substrates were determined with Rame-Hart contact angle goniometer (model 250).

3.   Results and Discussion

3.1. Structure and Microstructure

The XRD patterns of the single layer Ag film of 10 nm thickness shown in Fig. 1(a) reveals that the Ag has crystallized in to the FCC structure showing the (111), (200), (220) and (311) reflections and there is no evidence for crystalline silver oxide formation (fitted to JCPDS data card No. 65-2871). It has been shown earlier that bilayer geometry has a profound effect on the optical properties of metal-Si systems [18]. Hence, two types of bilayers of Ag and SnO_2 were prepared: (1) by depositing Ag first, to a desired thickness followed by the deposition of SnO_2 and (2) by depositing SnO_2 first, to a desired thickness followed by the deposition of Ag to the required thickness. The XRD patterns of the bilayer films in which both Ag and SnO_2 are 10 nm in thickness, are shown in Fig. 1(b) and (c). It is evident that there is no significant variation in crystallographic texture of the films, independent of the location of the metal layer (i.e. whether it is on top or bottom). It is noticed in both cases that there is no evidence for the crystallization of SnO_2.
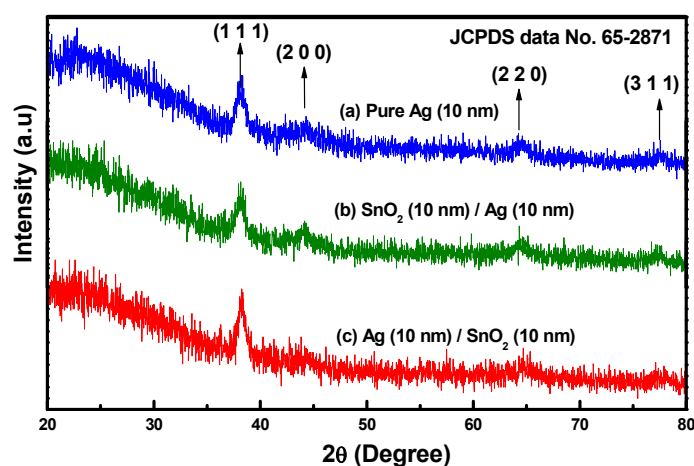

Figure 1. X-ray diffraction patterns of (a) Ag (10 nm), (b) Ag (10 nm)/SnO_2 (10 nm) and (c) SnO_2 (10 nm)/Ag (10 nm) films.

The atomic force microscopic (AFM) images of (a) bare glass substrate and (b) typical SnO_2 film are shown in Fig. 2. The bare glass substrate has a root mean square (r.m.s) roughness of 2.4 nm and the SnO_2 film has a r.m.s roughness of 3 μm. The AFM images of (a) Ag (10 nm), (b) Ag (10 nm)/SnO_2 (10 nm) and (c) SnO_2 (10 nm)/Ag (10 nm) films, respectively, are shown in Fig.3. It is evident that the films are rough and not very densely packed. The r.m.s roughness values are 0.84, 1.0 and 0.65 nm, respectively. It is observed that there is no correlation of roughness values with the nature of the film, *i.e.* whether it is single layer or bilayer and whether metal or dielectric is at the top. This is a consequence of the fact that thin film deposition at ambient temperature by thermal evaporation leads to large agglomerates due to low surface mobility of the adatoms. During thermal evaporation process, vapour (either metal or dielectric) atoms impinging onto the substrate have low

kinetic energy (few eV) and therefore, only surface diffusion is allowed leading to the formation of small stable clusters in the initial stages of growth (Volmer-Weber growth model). The number of clusters per surface unit (also known as cluster density) depends mainly on the diffusion length of the condensate atoms. Clusters then grow by capturing incoming atoms until a critical size or coverage is reached. After this stage, the growth is dominated by coalescence events, which produce larger clusters with lower density [19–23] as seen from the AFM images.
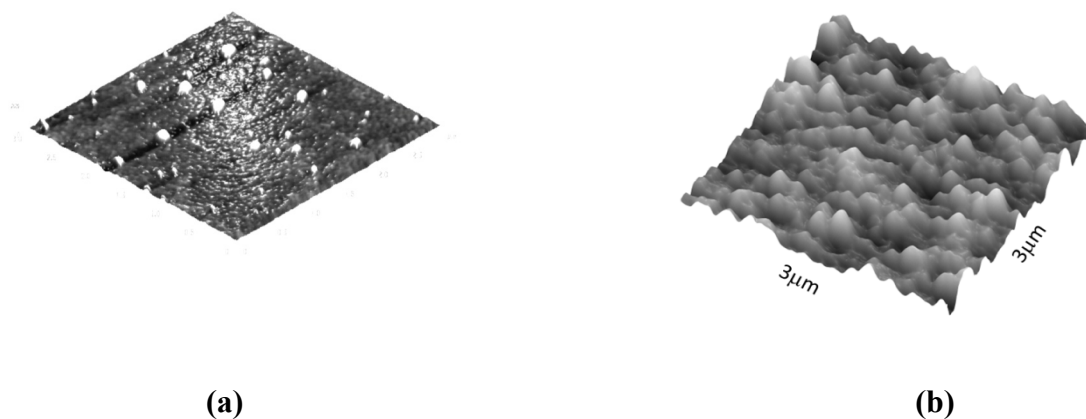

(a)   (b)

Figure 2. Atomic force microscopic (AFM) images of (a) bare glass substrate and (b) typical SnO_2 film.

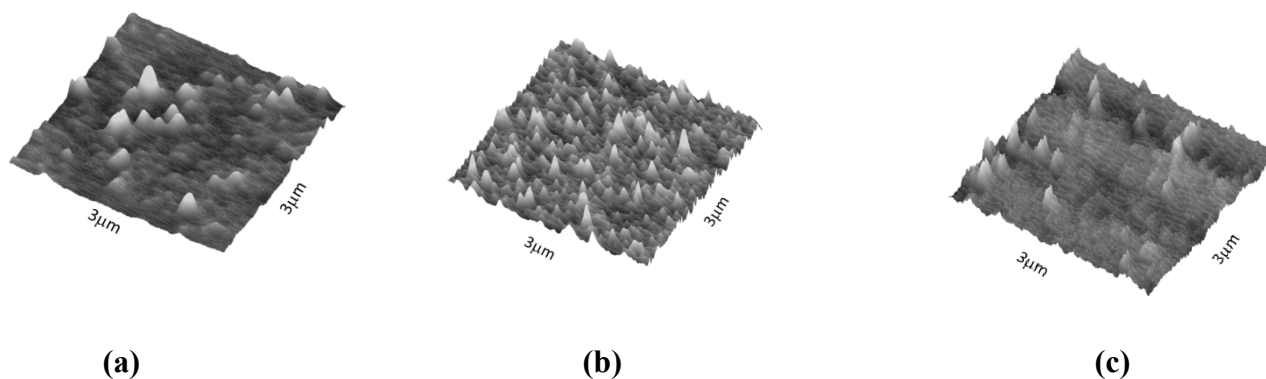(a)   (b)   (c)

Figure 3. Atomic force microscopy (AFM) images of (a) Ag (10 nm), (b) Ag (10 nm)/SnO_2 (10 nm) and (c) SnO_2 (10 nm)/Ag (10 nm) films.

The typical SEM micrograph of a 10 nm Ag film deposited on top of the SnO_2 film is shown in Fig. 4. It is evident from this figure that the Ag nanoparticles are lying on top of the SnO_2 layer, rather than mixing with it.

The growth of the films follows the structure zone models that have been used to describe the evolution of thin film microstructure as a function of surface adatom mobility [24,25]. At substrate temperatures (T_s) much lower than the melting point (T_m) of the elements the adatom mobility is insufficient for impacting vapour atoms to move on the substrates. The adatoms freeze instantly on impact on the substrate and subsequent atoms deposit on these initial layers leading to a columnar microstructure as observed in the AFM images as shown in Fig. 2. The melting points of Ag is 962 ^{o}C and that of SnO_2 is 1630 ^{o}C yielding values of 0.03 and 0.02, respectively, for the ratio of

T_s/T_m for deposition at ambient temperature. Therefore, as predicted by the structure zone models, the films exhibit the Zone 1 type of microstructure.
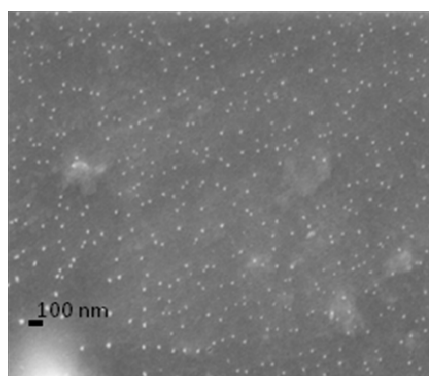

Figure 4. SEM image of an Ag+SnO$_2$ film showing the Ag nanoparticles on the SnO$_2$ underlayer.

3.2. Optical properties

The measured optical spectra of the pure Ag films of thicknesses ranging from 5 to 12 nm are shown in Fig. 5. It can be observed that, independent of thickness, there is a peak in transmission spectra centered around 320 nm. This is followed by a minimum centered around 660 nm in the case of the 5 nm film and 570 nm for the 8 nm thickness film. However, the 10 and 12 nm thickness films exhibit a very broad minimum in the measured range of wavelengths. The minimum in transmission spectra is attributed to the localized surface plasmon resonance (LSPR) of Ag. It is also observed that there is increase in the LSPR peak width with increasing thickness. This can be attributed to the fact that with increase in thickness there is an increase of particle size which is accompanied by change in particle shapes resulting in suppression of the LSPR peak.
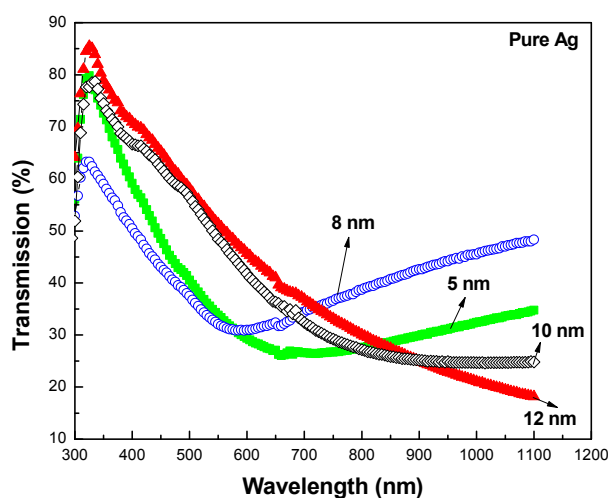

Figure 5. Measured spectral transmission curves of Ag films with different thickness.

To investigate impact of the dielectric constant of the media in which the Ag films are sandwiched, two experiments were carried out. In the first experiment, a buffer layer of SnO_2 of 10 nm thickness caps the Ag film. The Ag film is, thus, sandwiched between glass and SnO_2. The transmission spectrum of this sample is shown in Fig. 6 (Ag/SnO_2). It can be observed that, when a 10 nm SnO_2 film is deposited on a 5 nm Ag film, there is a dip centered around 600 nm. There is, thus, a blue shift in the LSPR peak in comparison to the 5 nm thickness Ag film deposited directly on silica substrate (in which case the LSPR peak was located at 660 nm). However, when the same SnO_2 film is deposited on the 10 nm Ag film, the LSPR peak is suppressed. The LSPR peak does not appear even when the SnO_2 layer (whose refractive index is higher than the glass substrate) is introduced between the glass and the 10 nm Ag film. In this case, the Ag film is sandwiched between SnO_2 and air (Fig. 6; SnO_2/Ag). In addition to this, both Ag and SnO_2 were co-evaporated simultaneously and observed that, there is no LSPR peak even in this case. It is thus inferred that only for Ag thickness ≤ 8 nm is a LSPR peak observed for Ag films whereas the critical thickness is 5 nm for Ag/SnO_2 films. The fact that, a 10 nm SnO_2 cap layer on a 5 nm Ag film supports the LSPR peak and is important for photovoltaic applications, since it can be used as a protective layer to suppress oxidation of the Ag layer. Initial studies showed that 10 nm thickness layers of ZnO and V_2O_5 (both of which have a higher refractive index than SnO_2) are able to support LSPR modes even when they are on top of a 10 nm Ag film, as shown in Fig. 7. This is further confirmation that appearance of LSPR peaks is sensitive to the dielectric environment around the Ag nanoparticles [26–32].
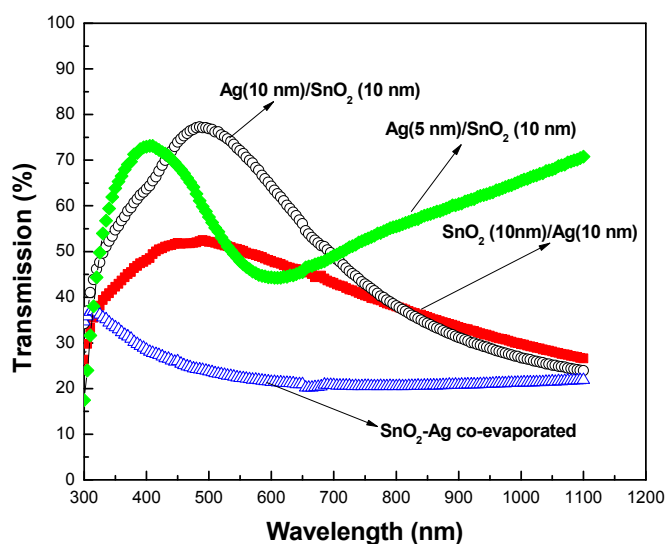

Figure 6. Measured spectral transmission curves of Ag/SnO_2 bilayer thin films.

The position and width of LSPR peaks are dependent on size, shape, fill factor and the depolarization factor of the nanoparticles [33,34,35]. At the initial stages of growth, Ag particles are separated but coalesce with the increment of thickness. Further increase in Ag thickness increases fill factor resulting in decreased inter particle separation. At smaller inter particle separations, coupling of charge oscillations between the particles becomes significant leading to shift of SPR peak [36,37].

The SPR peaks will also shift with increasing average dielectric constant of the surroundings as observed in the present study [38,39,40]. It has been shown earlier that there is a critical thickness below which interference effects do not suppress the LSPR [26]. The thickness of films in the present case is well below that limit and therefore, the possibility of the observed spectra arising due to interference has been neglected.
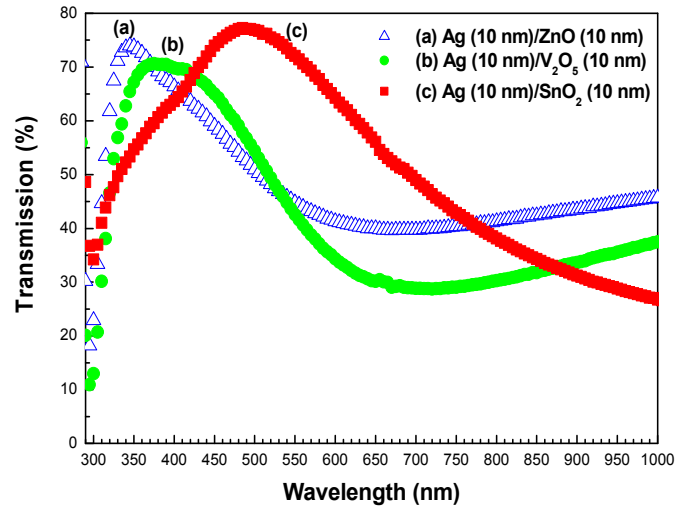

Figure 7. Measured spectral transmission of Ag/ZnO, Ag/V$_2$O$_5$ and Ag/SnO$_2$ films of 10 nm thickness each.

Briefly, the effective permittivity or dielectric constant of a composite medium given by the Maxwell-Garnett Mixing Rule as [41,42,43],

$$\varepsilon_{eff} = \varepsilon_h + \frac{\frac{1}{3}\sum_{i=1}^{n} f_{i*}(\varepsilon_{mi} - \varepsilon_h)\sum_{j=1}^{3}\frac{\varepsilon_h}{\varepsilon_h + N_{ij*}(\varepsilon_{mi} - \varepsilon_h)}}{1 - \frac{1}{3}\sum_{i=1}^{n} f_{i*}(\varepsilon_{mi} - \varepsilon_h)\sum_{j=1}^{3}\frac{N_{ij}}{\varepsilon_h + N_{ij*}(\varepsilon_{mi} - \varepsilon_h)}}$$

where ε_{eff} = effective dielectric constant of the composite medium

ε_h = dielectric constant of host medium

ε_{mi} = dielectric constant of ith type of metal particles in the host medium

f_i = filling fraction of the ith type of inclusion

n = number of different metal particles in the composite medium
j = 1, 2, 3 refers to the X, Y and Z Cartesian co-ordinates, and

N_{i1}, N_{i2} and N_{i3} refer to the depolarization factors of ith type of inclusion in the X, Y and Z directions. Depolarization factors are independent of size of the particle and type of the particle i.e. copper, silver and gold etc. Depolarization factors mainly depend on the shape of particles. If the particle shape is spherical then the depolarization factors are $\frac{1}{3}$, in each direction i.e.

$$N_1 = N_2 = N_3 = \frac{1}{3}$$

Independent of the shape of the particle, the sum of three depolarization factors should be one i.e. $N_1 + N_2 + N_3 = 1$. Based upon the shape of particles, two sets of depolarization factors exist, one set is for oblate ellipsoids (where major axis > minor axis) and other set is prolate ellipsoids (where major axis < minor axis),

Then the depolarization factor along j^{th} direction can be calculated as [7,8,9]

(j = 1, 2, 3 refers to the **X**, **Y** and **Z** direction**s**)

$$N_j = \int_0^\infty \frac{(D_1 D_2 D_3 du)}{2*(u + D_j^2)\sqrt{(u + D_1^2)(u + D_2^2)(u + D_3^2)}}, \quad j = 1, 2, 3$$

where, $u = \xi, \eta, \zeta$ are ellipsoidal co-ordinates, u is the scalar quantity which relates axial dimensions (D_1, D_2, D_3) with the Cartesian co-ordinates **X, Y** and **Z** as

$$\frac{X^2}{(u + D_1^2)} + \frac{Y^2}{(u + D_2^2)} + \frac{Z^2}{(u + D_3^2)} = 1$$

$$D_1 = D * (1 + \sqrt{1 - S}) \text{ and } D_2 = D * (1 - \sqrt{1 - S}), (D_2 = D_3)$$

S is the shape factor which is equal to 1 for spherical shape and decreases as particle shape deviates from spherical to more ellipsoidal shapes.

The simulated LSPR spectrum of an Ag film consisting of 50 nm diameter spherical particles (i.e. S = 1) and fill factor of 0.2 sandwiched between air and a medium of dielectric constant, $\varepsilon_h = 4$ (or refractive index = 2 as in the case for SnO_2) is shown in Fig. 8(a). It is evident that LSPR peak is broad with a width of about 100 nm. In the next simulation it was assumed that the Ag film consisted of 50% particles which are spherical (S = 1) and 25% each of particles with S = 0.9 and 0.8. In addition it was assumed that the individual filling fraction is 50%, 25% and 25% for S = 1, 0.9 and 0.8 respectively. Thus, for an overall filling fraction of 20%, 50% of the 20% consists of S = 1 particles and the remaining 50% is occupied by the ellipsoids (S = 0.9, 0.8) in equal ratio. The effect of such a distribution is quite remarkable as observed from Fig. 8(b). Apart from the main dipolar resonance at short wavelengths there are two other higher order resonances that are spectrally separated from each other which increases the effective peak width. With further increase in overall

filling fraction from 20% to 50%, keeping all other parameters same, there is further increase in width as seen from Fig. 8(c). Significantly, the extinction does not fall to zero on the long wavelength side of the peak, indicating "smearing" of the peak as observed in experimental results, in this study. Evidently, there is a match between simulation and trends of the experimental results in the present work. It would appear that the spectra observed experimentally, in the present work, are due to random distribution of shapes and fill fraction in the film.
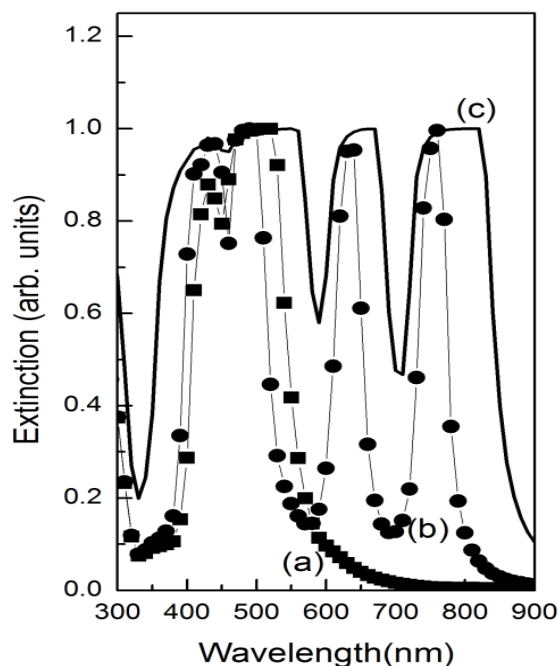

Figure 8. Simulated LSPR spectra for (a) Ag film with 50 nm diameter spherical particles (i.e. S = 1) and fill factor of 0.2 sandwiched between air and a medium of dielectric constant, $\varepsilon_h = 4$, (b) Ag film comprised of 50% particles which are spherical (S = 1) and 25% each of particles with S = 0.9 and 0.8. In addition it was assumed that the individual filling fraction is 50%, 25% and 25% for S = 1, 0.9 and 0.8, respectively, and an overall filling fraction of 20%, (c) for the same system as in (b) but an overall filling fraction of 50%.

Therefore, it can be inferred that the shifts in LSPR observed in the present are due to a combination of variation in size, shape and interparticle distance as well as the medium in which they are hosted (i.e. silica, SnO_2, ZnO or V_2O_5). It is necessary to fabricate patterned nanostructures to isolate the effect of each of these parameters.

3.3. Water repellant properties

In order to investigate the surface wettability of pure and metal doped film, the contact angle of water over these surfaces are measured. Contact angle can be related to the three interfacial tensions via Young's equation [44],

$$\cos\theta = \frac{Y_{SV} - Y_{SL}}{Y_{LV}}$$

where, Y_{SV} = Solid-vapor interfacial tension, Y_{SL} = Solid-liquid interfacial tension, Y_{LV} = Liquid-vapor interfacial tension.

Young's equation is developed for the case of an ideal solid surface which is relatively smooth. However, most thin film surfaces are not ideal and generally have finitely large surface roughness. Wenzel [45] modified Young's equation by taking into account the roughness of the surface. Then the apprarent contact angle can be related to true contact angle by

$$\cos\theta_W = r_W \left\{ \frac{Y_{SV} - Y_{SL}}{Y_{LV}} \right\} = r_W \cos\theta_Y$$

where, θ_W and θ_Y are the Wenzel and Young's contact angles and r_W is the Wenzel's roughness factor and may be defined as the ratio of the actual area of a rough surface to the geometric projected area.

The pure Ag films of 5 and 10 nm thickness showed average water contact angle of 103° and 105°, respectively. This indicates the hydrophobic nature of the films and confirms an earlier observation by some of the present authors that metallic films can indeed have hydrophobic surfaces due to partial oxidation. When a 10 nm SnO_2 layer is introduced between the 10 nm Ag film and substrate, the water contact angle decreases to 97° (i.e. SnO_2 is a buffer layer between Ag film and substrate). In contrast, when a 10 nm SnO_2 is deposited as a cap layer over the 10 nm Ag film, the decrease in water angle is only down to 104°. In earlier reports, it was shown that the water contact angle of SnO_2 films is of the order of 54–79° [12,13]. It can be seen from Table 1 that there is no change in the contact angle with the change in thickness of Ag.

Table 1. Contact angle data.

S.No.	Thin Film	Contact Angle (^{o})	Thickness of film (nm)
1	Ag on Glass	103	5
		105	10
2	SnO_2 on Glass	54-79 [ref]	20
3	Ag on SO_2 on Glass	97	Ag-10
			SnO_2-10
4	SnO_2 on Ag on Glass	104	Ag-10
			SnO_2-10

Evidently, compared to the single layer SnO_2 films there is increase in hydrophobicity in both cases. Wettability is dependent on both surface roughness and surface energy. The r.m.s surface roughness values are 10, 12 and 12 nm for the single layer Ag, 10 nm SnO_2 (or Ag) film on top of 10 nm Ag (or SnO_2) film, respectively. There is no correlation between surface roughness and

changes in the water contact angle. Interestingly, even when Ag and SnO_2 are co-evaporated the average contact angle is 94.5°, which is higher than that of the pure SnO_2, but lower than the pure Ag. It has been shown earlier that metal ion doping of SnO_2 can cause increase in contact angle [13]. It has been demonstrated previously that the increase in hydrophobicity of TiO_2 film with an Au metal buffer layer between TiO_2 and substrate can be attributed to the change in surface energy of the film [12]. This would appear to be the same cause for the observed increase in hydrophobicity when Ag (or SnO_2) is used as a buffer layer for SnO_2 (or Ag), in the present case. This is also the reason for the observed increase in contact angle when compared to the pure SnO_2 film. Thus, it is proposed that the films studied in the present work can be potentially used as anti-fogging transparent coatings for photovoltaic cells [17].

4. Conclusion

In summary, transparent single and bilayers of Ag and SnO_2 and Ag-SnO_2 composites have been deposited on glass substrates by thermal evaporation. The Ag films are crystalline and the morphology shows the presence of large clusters. Detailed optical studies indicate that the localized plasmon resonance peaks of Ag are thickness dependent. The location of the SnO_2 layer, i.e. whether it is underneath the Ag or caps it is extremely important in tuning the LSPR peak position and water contact angles. The wetting properties of Ag are independent of the thickness of the Ag film. The addition of Ag buffer layer beneath SnO_2 makes the material more hydrophobic. The addition of SnO_2 buffer layer lowers the contact angle. The change in wetting properties are due to change in surface energy of the material, modulated by the buffer layer and not due to surface roughness. These observations have potential for applications in self-cleaning surfaces.

Conflict of Interest

The authors declare that there are no conflicts of interest related to this study.

References

1. Simakov VV, Yakusheva OV, Grebennikov AI, et al. (2005) Current-voltage characteristics of thin-film gas sensor structures based on tin oxide. *Tech Phys Lett* 31: 339–340.
2. Tibucio-Silver A, Sanchez-Juarez A (2004) SnO_2: Ga thin films as oxygen gas sensor. *Mat Sci Eng B-Solid* 110: 268–271.

3. Batzill M, Diebold U (2005) The surface and materials science of tin oxide. *Prog Surf Sci* 79: 47–154.

4. Yu B, Zhu C, Gan F (1997) Exiciton spectra of SnO_2 nanocrystals with surficial dipole layer. *Opt Mater* 7: 15–20.

5. Menini P, Parret F, Gerrero M, et al.(2004) CO response of a nanostructured SnO_2 gas sensor doped with palladium and platinum. *Sens Actu B Chem* 103: 111–114.

6. Gupta S, Roy RK, Pal Chowdhury M, et al. (2004) Synthesis of SnO_2/Pd composite films by PVD route for a liquid petroleum gas sensor. *Vacuum* 75: 111–119.

7. Aguilar-Leyva J, Maldonado A, de La L Olvera M (2007) Gas sensing characteristics of undoped-SnO_2 thin films and Ag/SnO_2 and SnO_2/Ag. *Mater Charact* 58: 740–744.

8. Zhang J (1995) Silver clusters on SnO_2 thin film surfaces and their application to gas sensors. Ph.D Thesis, in the Department of Physics, Simon Fraser University.

9. Yu SH, Jia CH, Zheng HW, et al. (2012) High quality transparent conductive SnO_2/Ag/SnO_2 tri-layer films deposited at room temperature by magnetron sputtering. *Mater Lett* 85: 68–70.

10. Yu S, Zhang W, Li L, et al. (2014) Optimization of SnO_2/Ag/SnO_2 tri-layer films as transparent composite electrode with high figure of merit. *Thin Solid Films* 552: 15–154.

11. Dhar Purkayastha D, Pandeeswari R, Madhurima V, et al. (2013) Metal buffer layer mediated wettability of nanostructured TiO_2films. *Mater Lett* 92: 151–153.

12. Dhar Purkayastha D, Ghanashyam Krishna M, Madhurima V (2014) Molybdenum doped tin oxide thin films for self-cleaning applications. *Mater Lett* 124: 21–24.

13. Dhar Purkayastha D, Brahma R, Madhurima V, et al. (2015) Effects of metal doping on photoinduced hydrophilicity of SnO_2 thin films. *Bulletin Mater Sci* 38: 203–208.

14. Nakajima A, Abe K, Hashimoto K, et al. (2000) Preparation of hard super-hydrophobic films with visible light transmission. *Thin Sol Films* 376: 140–143.

15. Leem JW, Song YM, Yu JS (2011) Broadband wide-angle antireflection enhancement in AZO/Si shell/core subwavelength grating structures with hydrophobic surface for Si-based solar cells. *Opt Express* 19: A1155.

16. Manakasettharn S, Hsu T, Myhre G, et al. (2012) Transparent and superhydrophobic Ta_2O_5nanostructured thin films. *Opt Mat Exp* 2: 214–221.

17. Marco F, Lionel N, Boissière C, et al. (2010) Hydrophobic, Antireflective, Self-Cleaning, and Antifogging Sol−Gel Coatings: An Example of Multifunctional Nanostructured Materials for Photovoltaic Cells. *Chem Mater* 22: 4406–4413.

18. Mohiddon AM, Krishna GM (2013) Crystallite size and film–substrate interface mediated structural evolution of silicon thin films. *J Phy Chem Solids* 74: 1249–1253.

19. Campbell CT (1997) Ultrathin metal films and particles on oxide surfaces: structural, electronic and chemisorptive properties. *Surf Sci Rep* 27: 1–111.

20. Venables JA, Spiller JDT, Handbucken M (1984) Nucleation and growth of thin films. *Rep Prog Phys* 47: 399.

21. Henry CR (1998) Surface studies of supported model catalysts. *Surf Sci Rep* 31: 235–325.

22. Carrey J, Maurice JL, Petroff F, et al. (2002) Growth of Au clusters on amorphous Al_2O_3: are small clusters more mobile than atoms? *Surf Sci* 504: 75–82.

23. Toudert J, Cameli D, Denanot MF (2005) Morphology and surface-plasmon resonance of silver nanoparticles sandwiched between Si_3N_4 and BN layers. *J Appl Phys* 98: 114316.

24. Thornton JA (1977) High rate thick film growth. *Ann Rev Mater Sci* 7: 239–260.

25. Barna PB, Adamik M (1998) Fundamental structure forming phenomena of polycrystalline films and the structure zone models. *Thin Solid Films* 317: 27–33.

26. Brahma R, Ghanashyam KM (2011) Optical behavior of silver/dielectric and gold/dielectric bilayer thin films. *Physica E* 43: 1192–1198.

27. Brahma R, Ghanashyam KM (2012) Interface controlled growth of nanostructures in discontinuous Ag and Au thin films fabricated by ion beam sputter deposition for plasmonic application. *Bull Mater Sci* 35: 551–560.

28. Hu J, Cai W, Liu P, et al. (2010) Evolution of Surface Plasmon Resonance for Silver Particle Film on Mesoporous SiO_2 and Soda-Lime Glass During Heating in Air and H_2. *J Nanosci Nanotechnol* 10: 5369–5373.

29. Politano A, Formoso V, Chiarello G (2010) Plasmonic Modes Confined in Nanoscale Thin Silver Films Deposited onto Metallic Substrates. *J Nanosci Nanotechnol* 10: 1313–1321.

30. Baek KH, Kim JH, Lee KB (2010) Surface Plasmon Resonance of Tuning of Silver Nanoparticle Array Produced by Nanosphere Lithography through Ion Etching and Thermal Annealing. *J Nanosci Nanotechnol* 10: 3118–3122.

31. Murray WA, Suckling JR, Barnes WL (2006) Overlayers on Silver Nanotriangles: Field Confinement and Spectral Position of Localized Suface Plasmon Resonances. *Nano Lett* 6: 1772–1777.

32. Evanoff DD, Chumanov G (2005) Synthesis of optical properties of silver nanoparticles and arrays. *Chem Phys Chem* 6: 1221–1231.

33. Joerger R, Gampp R, Heinzel A, et al. (1998) Optical properties of inhomogeneous media. *Sol Eng Mater Sol Cells* 54: 351–361.

34. Moiseev SG (2009) Optical properties of a Maxwell-Garnett composite medium with nonspherical silver inclusions. *Russian Phys J* 52: 1121–1127.

35. Protopapa ML (2009) Surface Plasmon resonance of metal nanoparticles sandwitched between dielectric layers: theoretical modeling. *Appl Optics* 48: 778–785.

36. Reinhard BM, Siu M, Agarwal H (2005) Calibration of Dynamic Molecular Rulers based on Plasmon Coupling between Gold nanoparticles. *Nano Lett* 5: 2246–2252.

37. Verma S, Tirumala RB, Rai S (2012) Influence of parameters on surface plasmon resonance characteristics of densely packed gold nanoparticle films grown by pulsed laser deposition. *Appl Surf Sci* 258: 4898–4905.

38. Wang J-F, Li H-J, Zhou Z-Y, et al. (2010) Tunable surface-plasmon-resonance wavelength of silver island films. *Chin Phys B* 19: 117310

39. Xu G, Tazawa M, Jin P, et al. (2005) Surface Plasmon resonance of sputtered Ag films: Substrate and mass thickness dependence. *Appl Phys A* 80: 1535–1540.

40. Kelly KL, Coronado E, Zhao LL, et al. (2003) The Optical Properties of Metal Nanoparticles: The Influence of size, shape, and Dielectric Environment. *J Phys Chem B* 107: 668–677.

41. Cecilia Noguez (2007) Surface Plasmons on Metal Nanoparticles: The Influence of Shape and Physical Environment. *J Phys Chem C* 111: 3806–3819.

42. Koledintseva MY, DuBroff RE, Schwartz RW (2006) A Maxwell Garnett Model for Dielectric Mixtures containing conducting particles at Optical Frequencies. *Prog Electromag Res PIER* 63: 223–242.

43. Kolrdintseva MY, Wu J, Zhang J (2004) Representation of permittivity for multi-phase dielectric mixtures in FDTD modeling. *Proc Inter Symp Electromag Compat (EMC)* 1: 309–314.

44. Young T (1805) An Essay on cohesion of solids. *Philos Trans R Soc London* 95: 65–87.

45. Wenzel RN (1936) Resistance of solid surfaces to wetting by water. *Ind Eng Chem* 28: 988–994.